Supplemental Data

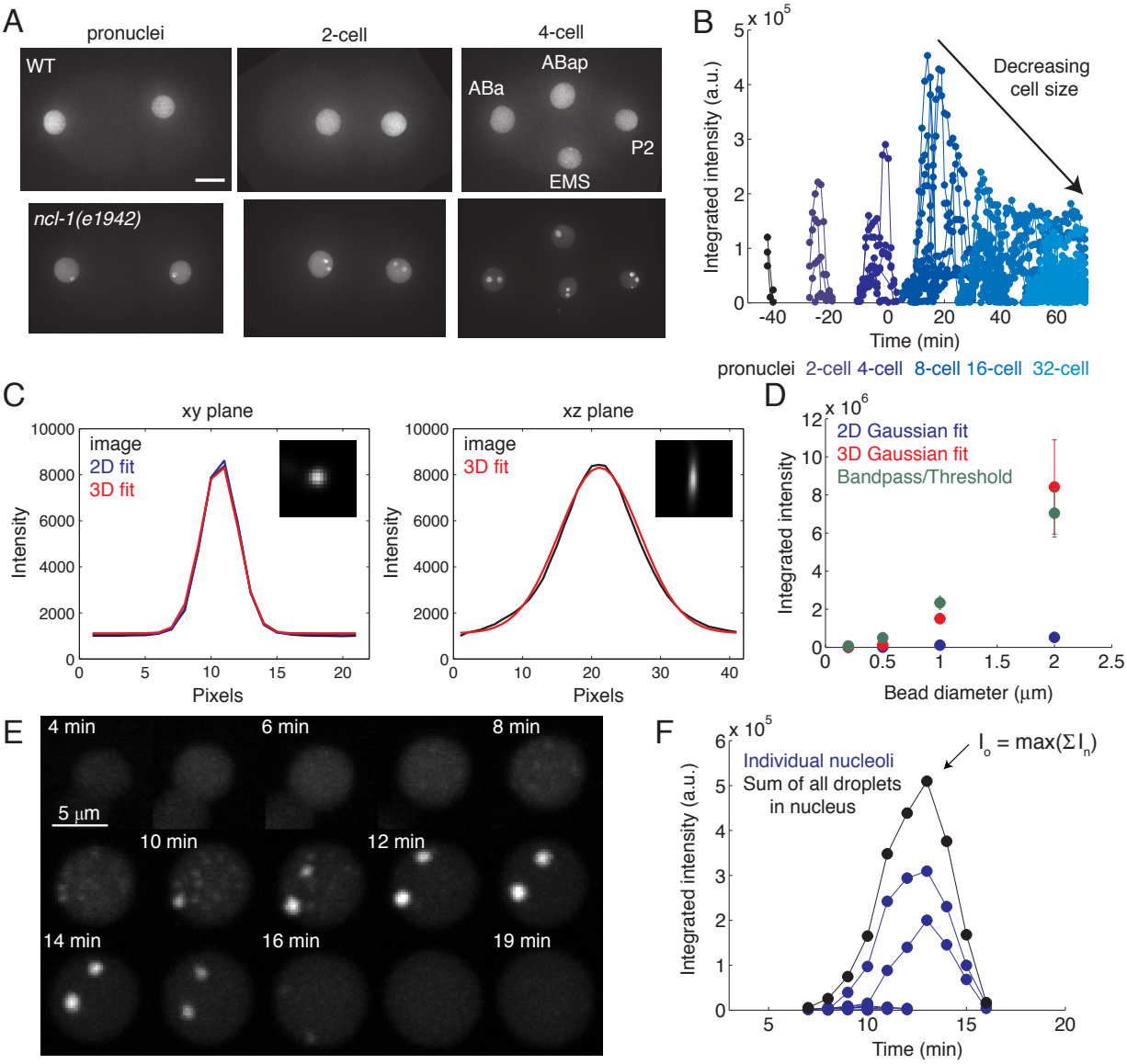

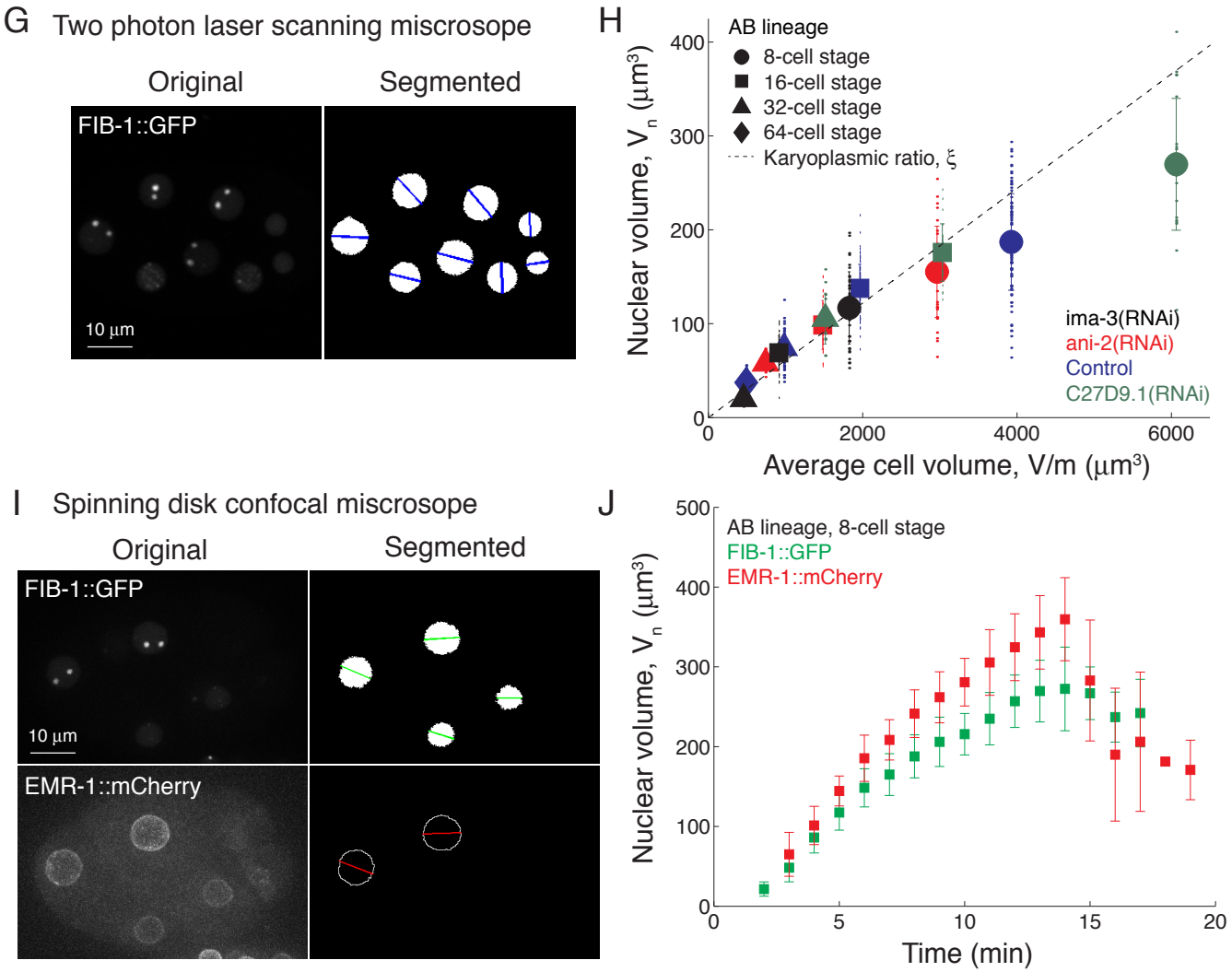

Figure S1, related to Figure 1.

Quantifying nucleolar size and nuclear volume in early *C. elegans* embryos.

(A) Maximum intensity projections of 3D stacks of wild-type (WT) and *ncl-1(e1942)* mutant embryos expressing FIB-1::GFP at the pronuclear, 2- and 4-cell stages. Note that nucleoli assemble in all nuclei in *ncl-1* mutants, but not until EMS (Table S1) and only robustly in the 8-cell stage in WT. Scalebar = 10 µm.

(B) Integrated intensity in arbitrary units of individual nucleoli as a function of time in a developing *ncl-1(e1942)* embryo. Colors correspond to cell stage as indicated below. Time was measured relative to nuclear envelope breakdown in cells ABa and ABp.

(C) Intensity profiles of a 1 µm bead in the xy and xz planes. 2D and 3D Gaussian fits are shown.

(D) Comparison of the integrated intensity beneath a 2D or 3D Gaussian fit with our bandpass/threshold method for 0.2, 0.5, 1 and 2 µm beads.

(E) A montage of maximum intensity projections of a single 8-cell stage nucleus (ABpl from Figure 1A) over time.

(F) The integrated intensity, calculated using a bandpass filter and threshold, of individual nucleoli (blue) and the sum over all nucleoli and FIB-1::GFP foci (black) as a function of time for the nucleus shown in Figure S1E. We define the maximum nucleolar intensity, I_o, as the maximum value of the sum.

(G) Maximum intensity projections of the original and segmented images of the 8-cell stage embryo expressing FIB-1::GFP shown in Figure 1A. These images were acquired on a two photon laser scanning microscope. Nuclei were segmented using Otsu thresholding and the diameter (blue lines) was used to calculate nuclear volume.

(H) The karyoplasmic ratio is approximately constant for 8 to 64-cell stage embryos across all RNAi conditions. Nuclear volume of the AB lineage in 8 to 64-cell stage embryos imaged on a two photon laser scanning microscope is plotted as a function of average cell volume. The x-axis is an approximation of cell size, assuming that the embryo volume V is divided into m cells of equal size. The dashed line represents the karyoplasmic ratio calculated independently from the ratio of concentrations in the cytoplasm following nuclear envelope breakdown and the nucleoplasm prior to nucleolar assembly: $\xi = C_{cell}/C_n = 0.061$. Large embryos at the 8-cell stage exhibit a slightly smaller karyoplasmic ratio, consistent with a previous report [S1].

(I) Maximum intensity projections of the original and segmented images of an 8-cell stage embryo expressing both FIB-1::GFP (nucleoli) and EMR-1::mCherry (nuclear membrane). These images were acquired on a spinning disk confocal microscope, which enables dual-color acquisition but suffers from attenuation such that only ~half the embryo can be visualized. Nuclei were segmented using Otsu thresholding for FIB-1::GFP images and a marker-based watershed algorithm for EMR-mCherry images.

(J) A comparison of the nuclear volume calculated using each marker for n = 10 AB, 8-cell stage nuclei.

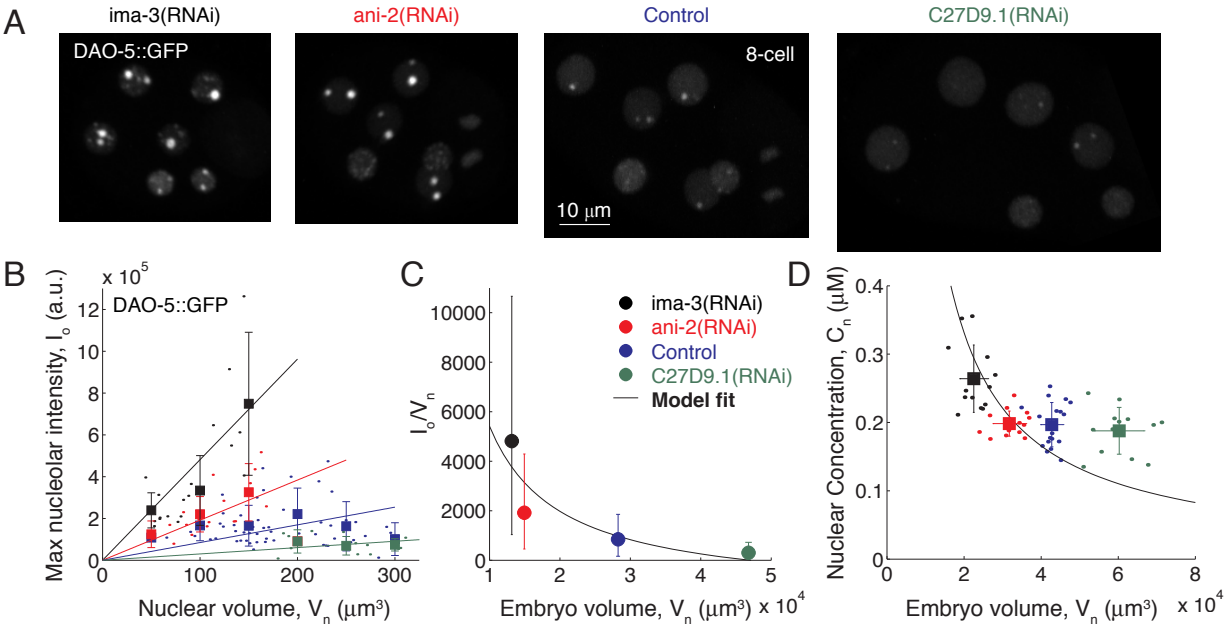
A
ima-3(RNAi)
ani-2(RNAi)
Control
C27D9.1(RNAi)
DAO-5::GFP
8-cell
10 µm
B
x 10^5
DAO-5::GFP
Max nucleolar intensity, I_o (a.u.)
Nuclear volume, V_n (µm³)
C
I_o/V_n
ima-3(RNAi)
ani-2(RNAi)
Control
C27D9.1(RNAi)
Model fit
Embryo volume, V_n (µm³) x 10^4
D
Nuclear Concentration, C_n (µM)
Embryo volume, V_n (µm³) x 10^4

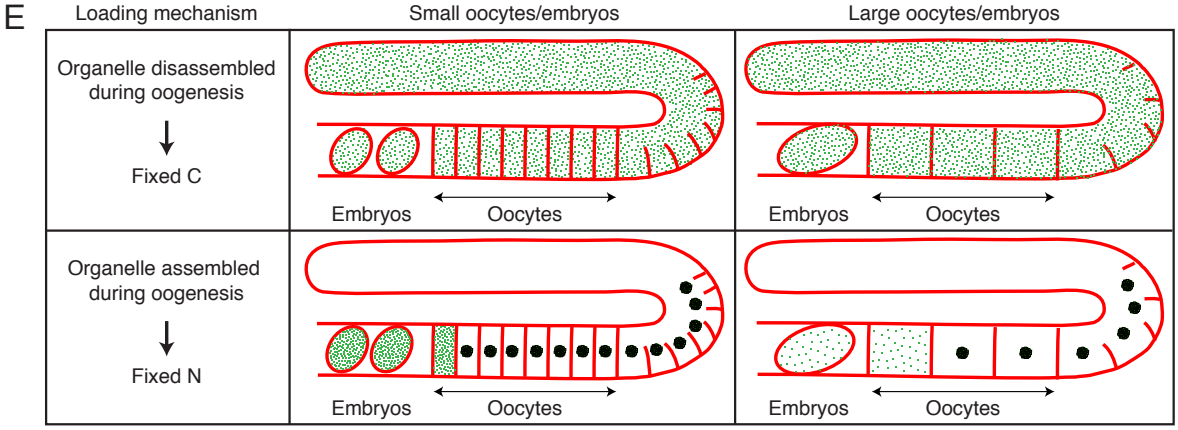
E
Loading mechanism
Small oocytes/embryos
Large oocytes/embryos
Organelle disassembled during oogenesis
Fixed C
Organelle assembled during oogenesis
Fixed N
Embryos
Oocytes

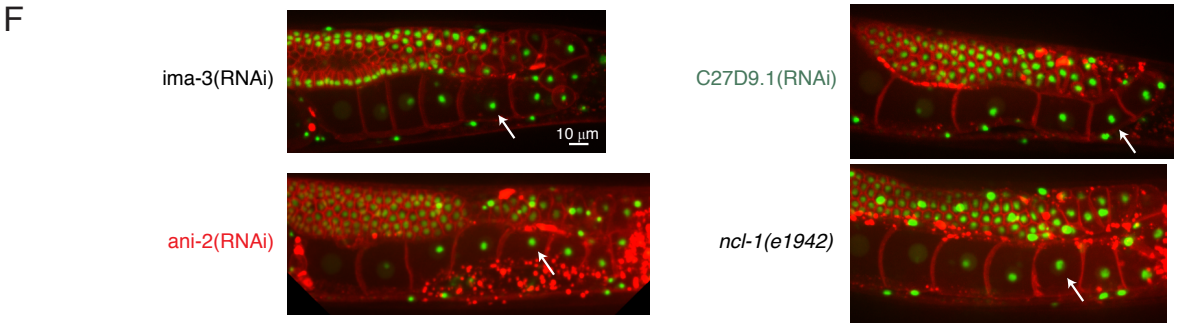
F
ima-3(RNAi)
ani-2(RNAi)
C27D9.1(RNAi)
ncl-1(e1942)
10 µm

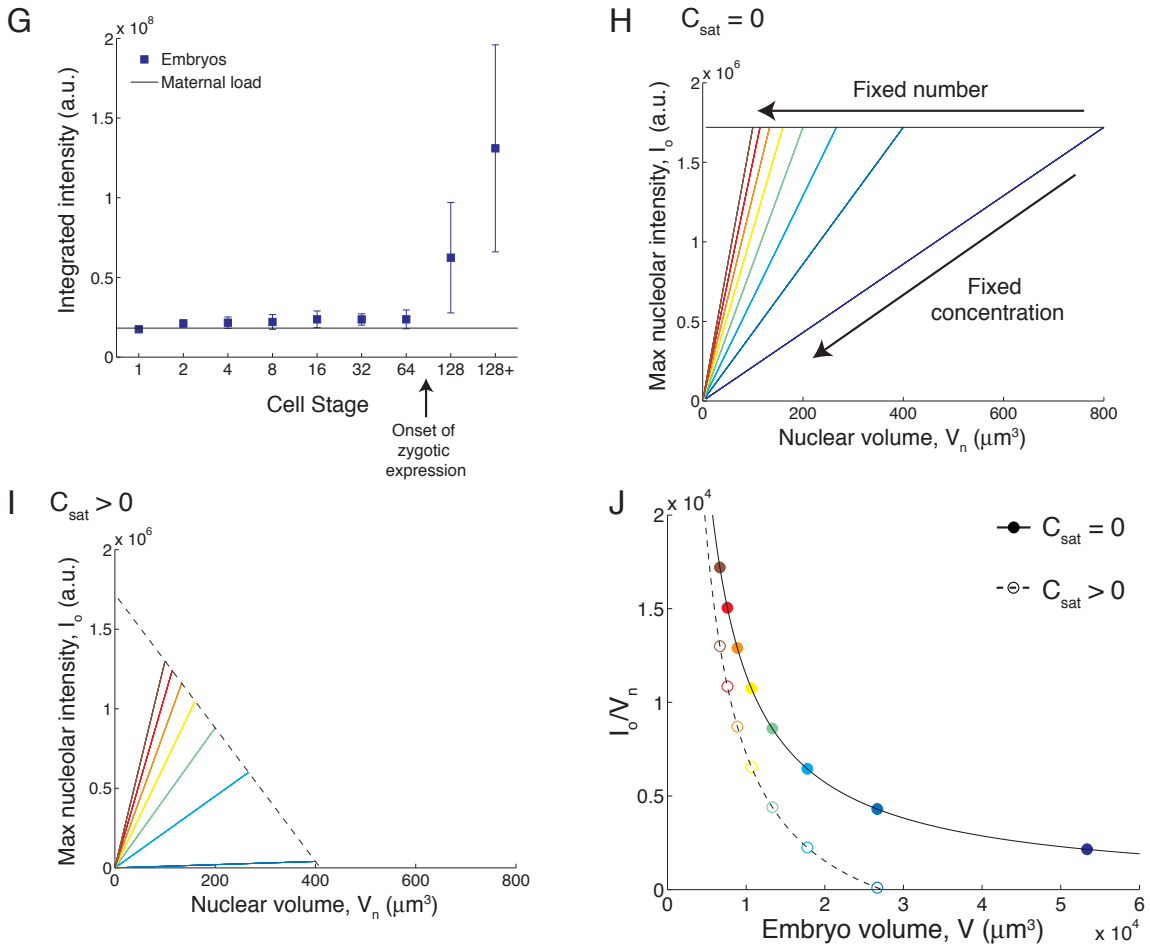

Figure S2, related to Figure 3.

Maternal loading of an assembled nucleolus gives rise to direct and inverse scaling regimes for FIB-1::GFP and additional nucleolar marker DAO-5::GFP.

(A) Maximum intensity projections of 3D stacks of embryos expressing DAO-5::GFP at the 8-cell stage following RNAi treatment.

(B) Direct scaling of maximum nucleolar intensity with nuclear volume during development in each RNAi condition; inverse scaling across RNAi conditions for embryos expressing DAO-5::GFP. Raw data (points) and mean ± standard deviation across 50-μm bins (squares) are shown. Raw data for each RNAi condition were fit to a line through the origin to determine the slope, I_o/V_n. n = 3 embryos per RNAi condition.

(C) Fitted slopes from panel B are plotted as a function of mean embryo volume for each RNAi condition. Error bars are 95% confidence intervals. Raw data was fit to the master scaling equation, $I_o = \alpha[N/(V\xi)-C_{sat}]V_n$, with αN and αC_{sat} as free parameters (solid line).

(D) Nuclear concentration of DAO-5::GFP decreases with increasing embryo volume. Raw data (points) and mean ± standard deviation for each condition (squares) are shown with a fit to the equation $C_n = N/(\xi V)$.

(E) Schematic diagram illustrating the consequences of organelle loading. When an organelle is disassembled during oogenesis, the concentration of components is fixed across oocytes of different size. When an organelle is assembled during oogenesis, the number of components is fixed across oocytes of different size, leading to differences in concentration.

(F) Maximum intensity projections of oocytes in the hermaphrodite gonad for each RNAi condition and the *ncl-1(e1942)* mutant. Red channel is mCherry::PH(PLC1δ1); green channel is FIB-1::GFP. White arrows indicate the intact nucleolus loaded into an oocyte.

(G) The fluorescence intensity of FIB-1::GFP loaded into oocytes ("maternal load") can account for the total fluorescence intensity found throughout the embryo from the 1 to 64-cell stages. Evidence of zygotic expression can be seen beginning at the 128-cell stage, where fluorescence intensity dramatically increases. n = 10-15 embryos per stage.

(H) Analytical results from the concentration-dependent phase transition model. With no partitioning ($C_{sat} = 0$, such that the organelle is an infinite sink for components), the fixed concentration constraint leads to direct scaling with nuclear volume, while the fixed number constraint results in a constant organelle size, independent of nuclear volume. Color corresponds to embryo size.

(I) When $C_{sat} > 0$, the nucleoplasmic pool limits organelle assembly in large nuclei, giving rise to an inverse scaling regime.

(J) The apparent concentration, I_o/V_n, decreases as a function of embryo volume. The decreases occurs more dramatically when $C_{sat} > 0$.

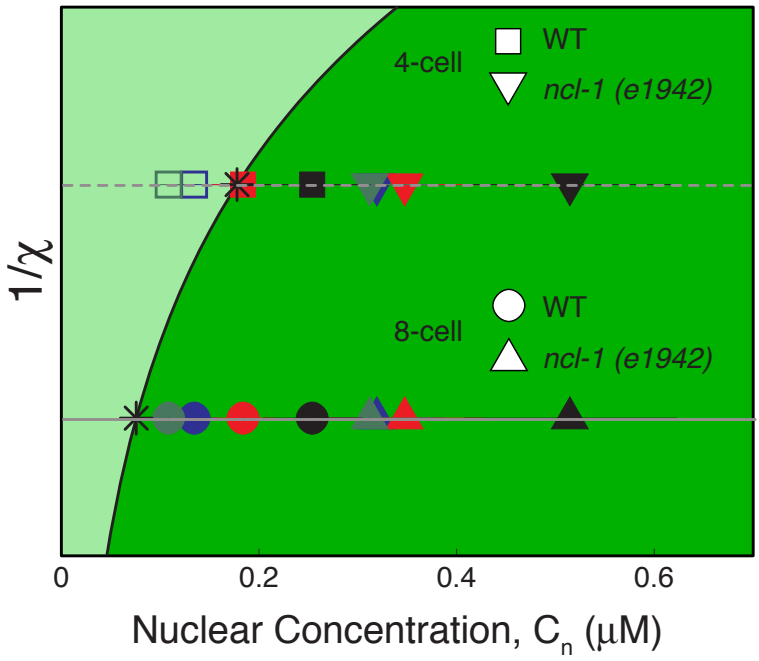

Figure S3, related to Figure 4.

Phase diagram for nucleolar assembly. *ncl-1* embryos fall above the phase boundary in all developmental stages and all RNAi conditions.

Table S1, related to Figure 4.

Fraction of embryos (%) with nucleoli assembled in each lineage at the 4-cell stage.

Condition	ABa/ABp	EMS	P2
L4440 (RNAi), negative control	0/30 (0%)	30/30 (100%)	8/30 (27%)
ani-2 (RNAi)	15/28 (53%)	28/28 (100%)	16/28 (57%)
ima-3 (RNAi)	26/26 (100%)	26/26 (100%)	26/26 (100%)
C27D9.1 (RNAi)	0/25 (0%)	7/25 (28%)	3/25 (12%)
ncl-1(e1942)	24/24 (100%)	24/24 (100%)	24/24 (100%)

Supplemental Experimental Procedures

Construction of transgenic worm lines:

GFP-tagged fosmid lines were kindly provided by Tony Hyman (MPI-CBG) [S2]. To visualize the nuclear envelope, emr-1 was amplified from genomic DNA and cloned into plasmid TH313 [S3], which contains the *pie-1* promoter and a C-terminal mCherry tag, using SpeI and SmaI restriction sites. This construct was randomly integrated into the worm genome by microparticle bombardment [S4].

Transgenic *C. elegans* lines

Strain Name	Genotype	Source
CPB001	fib-1::gfp	[S2]; clone 445429768005125 D03
	https://transgeneome.mpi-cbg.de/transgeneomics/public/clone.html?wellId=32516341	
CF2218	ncl-1(e1942)	CGC
OD70	mCherry::PH(PLC1δ1)	CGC
CPB008	CPB001xCF2218	cross
CPB009	CPB001xOD70	cross
CPB011	dao-5::gfp	[S2]; clone 37513532900044066 A01
	https://transgeneome.mpi-cbg.de/transgeneomics/public/clone.html?wellId=32556468	
CPB065	ptnIs035[Ppie1::emr-1::mCherry + Cbunc-119(+)]	
CPB064	CPB001xCPB065	

Worm maintenance and imaging:

C. elegans lines were maintained at 20^{o}C on NGM plates seeded with OP50 bacteria. Embryos were dissected from gravid hermaphrodites and imaged on M9-agarose pads. Oocytes were imaged in adult hermaphrodites anesthetized with 1% levamisole hydrochloride in M9.

Timelapse movies and still images were acquired on a two-photon laser scanning system custom-built around an upright Olympus BX51 microscope. An excitation wavelength of 960 nm was used to visualize GFP while maintaining embryo viability. Emitted light was collected with a 40X/NA0.8 water immersion objective and an NA1.3 oil immersion condenser and detected with high quantum efficiency GaAsP photomultiplier tubes (Hammamatsu). 3D volumes were acquired using an objective piezo controlled by ScanImage software [S5].

Images of dual-labeled worm lines were taken on an inverted Zeiss Axio Observer Z1 microscope equipped with a Yokogawa CSU-X1 confocal spinning disk (Intelligent Imaging Innovations) and a QuantEM 512SC camera (Photometrics). Oocytes were imaged with a 40X/NA1.4 oil immersion objective; embryos were imaged with a 100X/NA1.4 oil immersion objective.

RNAi experiments were performed by picking L4 larvae onto NGM plates containing 1 mM IPTG and 100 μg/mL ampicillin, seeded with feeding clones from the Ahringer library [S6]. The

empty vector L4440 served as a negative control for all experiments. Worms were allowed to feed and grow at 20°C for 36-48 hrs before embryos were harvested for imaging. Knockdown of *ima-3* results in embryonic lethality [S7]. After 36 hrs on *ima-3* RNAi feeding plates, hermaphrodites contain small embryos that successfully complete early divisions in which FIB-1::GFP and DAO-5::GFP enter and exit the nucleus. However, all of these embryos fail to hatch.

RNAi feeding clones

Gene Name	Sequence
negative control	L4440
ani-2	K10B2.5
ima-3	F32E10.4
-	C27D9.1
ncl-1	ZK112.2

Image analysis:

Images were analyzed with custom software in Matlab. Nucleoli were detected by first convolving the raw z-stacks with a 3D bandpass filter. A Gaussian kernel was used to smooth high-frequency noise. A low-frequency boxcar kernel was used to remove objects larger than the largest nucleolus typically observed in *ima-3(RNAi)* embryos. The difference between the low-pass and high-pass images was thresholded; the threshold value was determined empirically to retain small/dim nucleoli while minimizing detection of background/autofluoresence as much as possible. The same kernel sizes and threshold value were used for all RNAi conditions acquired on the same microscope (i.e. same values for all movies taken on the two photon; different values for all images taken on the spinning disk). The integrated intensity of a nucleolus was calculated by summing the fluorescence intensity within each detected object. Comparison of our method to 2D and 3D Gaussian fits of beads is shown in Figure S1D. 3D gaussian fitting of nucleoli was not robust and frequently failed to converge or expanded to fit the entire nucleus.

The maximum nucleolar intensity per nucleus, I_o, was obtained by taking the maximum value of the sum of integrated intensities for all nucleoli within a nucleus (see Figure S1F).

Nuclei were segmented using Otsu thresholding of FIB-1::GFP or DAO-5::GFP fluorescence. To validate this approach, we crossed an EMR-1::mCherry line into our FIB-1::GFP line to directly visualize the nuclear envelope. We used a marker-based watershed algorithm to segment the nuclear envelope. Nuclear volume was calculated using the diameter (d) extracted from the image plane with the largest nuclear area and assuming spherical geometry: $V_n = 4\pi(d/2)^3/3$. Results from both markers are shown in Figure S1J. FIB-1::GFP measurements are lower than EMR-1::mCherry, but these more accurately reflect the volume within which the soluble pool of nucleolar components resides.

The integrated intensity in the nucleoplasm was determined by subtracting the sum of the integrated intensities of all nucleoli and FIB-1::GFP foci (as shown in Figure S1F) from the total intensity inside segmented nuclei.

Embryo volume was calculated using the length (l) and width (w) of the eggshell at the mid-plane and assuming ellipsoidal geometry: $V = \pi l w^2/6$. These measurements were made at the 4-cell stage; however, embryo volume does not change with time or cell stage.

Nuclear concentration, C_n, was measured by calculating the average pixel intensity in nuclei of 4-cell stage embryos prior to nucleolar assembly (if any). Pixel intensity was converted to concentration units as described below.

Calibrating pixel intensity:

His-tagged FIB-1::GFP was purified from *E. coli* using standard Ni affinity chromatography procedures. Protein concentration was determined by a Bradford assay and confirmed spectrophotometrically. A dilution series of purified protein was imaged with the same acquisition settings as embryos and used to generate a standard curve, $I = a[\text{FIB-1::GFP}]$. The slope of this curve, $a = 3.1 \times 10^3$ intensity/pixel/μM, was used to estimate the nuclear concentration, C_n; the number of FIB-1::GFP molecules per embryo, N; and the saturation concentration, C_{sat} (see below).

Phase Transition Model:

We consider the nucleus as a two-phase system containing a mixture of the bulk nucleoplasm and the nucleolus. At the beginning of each cell cycle, these two liquid phases are fully mixed, with nucleolar components dissolved throughout the nucleoplasm. As the cell cycle progresses, the nucleoplasm undergoes a de-mixing phase transition in which nucleolar components condense to form a distinct phase: the nucleolus. The maximum size of the nucleolus is reached when the concentration of nucleolar components remaining in the nucleoplasm is reduced to the saturation concentration, C_{sat}.

We make two simplifying assumptions before examining the scaling predictions of this model. First, the surface tension, γ, of nucleolar droplets is small and can be ignored. Surface tension represents an energetic cost of creating an interface, and can contribute to both the kinetics of droplet assembly and the equilibrium size of droplets. However, γ is expected to be small for macromolecular liquid phases; γ for nucleoli in *X. laevis* germinal vesicles was estimated to be ~10 μN/m [S8], which is 10^4-fold smaller than the air-water interface. Thus, here we ignore the effect of the surface energy on nucleolar assembly.

Second, this model assumes that the de-mixing phase transition in the nucleoplasm approaches equilibrium. The cell cycle in early embryos progresses rapidly, ~20 min for the AB lineage at the 8-cell stage, and we do not observe a long plateau in nucleolar intensity for these early stages (Figure 1B). This raises the possibility that the nucleoplasm does not have sufficient time to reach equilibrium before the cell divides. However, we frequently see plateaus in nucleolar intensity in the posterior lineages of the 16-cell stage and all lineages of the 32 and 64-cell stage, suggesting that equilibrium has been reached in these later, longer cell cycles. If nucleoli in the 8-cell stage have not fully equilibrated, then the observed maximum nucleolar intensity will be

less than that predicted by our model. This could contribute to the variability observed in nucleolar size at the 8-cell stage.

Under these assumptions, the maximum size of the nucleolar phase is determined by the supersaturation of the nucleoplasm. When the nucleoplasm is undersaturated, $C_n < C_{sat}$, nucleoli do not assemble and nucleolar components remain dissolved throughout the nucleoplasm. When the nucleoplasm is supersaturated, $C_n > C_{sat}$, nucleolar components in the nucleoplasm condense into nucleolar droplets, depleting the nucleoplasm until its concentration reaches saturation, $C_n \approx C_{sat}$. Thus, the size of the nucleolus depends on the degree of supersaturation: $C_n - C_{sat}$. To compare directly with experiments, we express the size of the condensed phase in terms of intensity, such that $I_o = \alpha[C_n - C_{sat}]V_n$, where α is the intensity per molecule.

Now we examine the scaling behavior of the nucleolar phase as a function of nuclear volume under two different constraints. First, we fix the *concentration* of nucleolar components, C, to simulate development. Second, we fix the *number* of nucleolar components, N, to simulate maternal loading of an intact nucleolus into oocytes of different size following RNAi.

1. Within a developing embryo, nucleolar components are dispersed at mitosis and allocated proportionately to daughter cells, yielding a constant concentration of nucleolar components within cells of different size. Thus, the total concentration of molecules within any given blastomere is the same as the total concentration in the embryo, $C_{cell} = C$. However, these molecules are concentrated into the nucleus, yielding a nucleoplasmic concentration, $C_n = C/\xi$. The nucleolus then assembles to a size given by

$$I_o = \alpha\left[\frac{C}{\xi} - C_{sat}\right]V_n. \qquad \text{Eq. 1}$$

Since C, ξ and C_{sat} are roughly constant from the 8 to 64-cell stage in a developing embryo, we predict a direct scaling between nucleolar size and cell size: $I_o \sim V_n \sim V_{cell}$.

2. Across RNAi conditions, N is fixed, rather than C. We can express C in terms of N and V to obtain a master scaling equation,

$$I_o = \alpha\left[\frac{N}{\xi V} - C_{sat}\right]V_n. \qquad \text{Eq. 2}$$

Since N is fixed, the scaling proportionality depends inversely on embryo volume. Thus, for a given cell/nucleus volume, larger embryos (larger V) will have smaller organelles and vice versa. The inverse scaling prediction can be seen more clearly when we look at a particular developmental stage. For example, $V = m*V_{cell} = m(V_n/\xi)$, where m = 8 for the 8-cell stage. Substituting into Eq. 2, we find

$$I_o = \alpha\left[\frac{N}{m} - C_{sat}V_n\right], \qquad \text{Eq. 3}$$

yielding a linear relationship between I_o and V_n with a negative slope, $-\alpha C_{sat}$.

In Figure S2H, we plot the results of our analytical model under the fixed C and fixed N conditions. Previous work has modeled organelle scaling using a limiting component model that treats the organelle as an infinite sink, into which all components eventually assemble [S9, S10]. In our model, this corresponds to the case where $C_{sat} = 0$. For this limit, organelle size scales directly with cell (nuclear) size when C is fixed. However, there is no scaling when N is fixed: organelle size is the same in all cells, regardless of their size (Figure S2H, Eq. 3). Therefore, the

simple limiting component model cannot account for the inverse size scaling observed experimentally across RNAi conditions.

Indeed, to obtain inverse scaling, C_{sat} must be greater than zero. When $C_{sat} > 0$, our model predicts direct scaling when C is fixed (albeit with a shallower slope) and inverse scaling when N is fixed (Figure S2I, Eq. 3), just as observed experimentally. The qualitatively distinct behavior that arises when $C_{sat} > 0$ highlights the novel feature of our model: namely, that the condensed organelle phase coexists with a soluble phase.

Finally, we plot the slope of the direct scaling curves as a function of embryo volume (Figure S2J). In both cases, the apparent organelle concentration, I_o/V_n, decreases with increasing embryo volume. However, I_o/V_n decreases more rapidly when $C_{sat} > 0$. This is because more components are required to maintain the saturation concentration in large nuclei compared to small nuclei, so fewer excess components are available to assemble into the organelle. Eventually, for very large embryos, the nucleoplasmic concentration falls below C_{sat} and no nucleolus assembles.

Estimating model parameters:

All model parameters were measured independently to produce a zero-free parameter prediction. Parameter values are reported in the following table and were estimated as described below.

Model Parameters

Parameter	Units	Measured (mean ± std)
α	intensity/molecule	39.4 ± 4.4
ξ	-	0.061 ± 0.004
N (method 1)	molecules	1.66 ± 0.11 x10^5
N (method 2)	molecules	1.52 ± 0.65 x10^5
C_{sat}	molecules/μm^3	43 ± 11
C_{sat}	µM	0.071 ± 0.02
$C_{sat}^{4\text{-cell}}$	molecules/μm^3	107 ± 25
$C_{sat}^{4\text{-cell}}$	µM	0.178 ± 0.04
N^{ncl1}	molecules	4.45 ± 0.45 x10^5

α, the intensity per molecule, was calculated from the slope of the standard curve of purified FIB-1::GFP, a. Voxel size was calculated using the axial width of the two-photon excitation volume [S11].

$\alpha = a*(1 \text{ pixel}/(0.22*0.22*2.7 \ \mu m^3) * 1 \ \mu M/(602 \text{ molecules}/\mu m^3) = 39.4$ intensity/molecule

The karyoplasmic ratio was estimated using the ratio of FIB-1::GFP concentration in the cytoplasm following nuclear envelope breakdown (such that nucleolar components were dispersed throughout the cell) and in the nucleoplasm prior to nucleolar assembly: $\xi = C_{cell}/C_n = 0.061$. This value is consistent with data from Hara and Kimura [S1], from which we estimate $\xi = 0.04$, assuming spherical geometries for both nuclei and cells.

Two methods were used to estimate the number of FIB-1::GFP molecules loaded per embryo. First, we fit an inverse function, $C_n = N/(\xi V)$, to the nuclear concentrations measured in embryos of different size (Figure 3C, main text): $N = 1.66 \pm 0.11 \times 10^5$.
Second, we directly measured the concentration in the cytoplasm following nuclear envelope breakdown and multiplied by embryo volume: $N = C_{cell}*V = 1.52 \pm 0.65 \times 10^5$.

To estimate C_{sat}, we directly measured the nucleoplasmic concentration in 8-cell stage embryos at the time point when nucleoli reached their maximum size, I_o. $C_{sat} = 43 \pm 11$ molecules/μm^3 = 0.071 ± 0.02 μM. Additionally, we measured $C_{sat}^{4\text{-cell}}$ in cells ABa and ABp in all *ima-3(RNAi)* embryos and in *ani-2(RNAi)* embryos that assembled nucleoli. $C_{sat}^{4\text{-cell}} = 107 \pm 25$ molecules/μm^3 = 0.178 ± 0.04 μM.

Limiting component:

It is important to recognize that while C_n and C_{sat} refer to FIB-1::GFP concentrations, FIB-1 is not necessarily an essential nucleolar component. Indeed, as a consequence of intact nucleolus loading, the concentration of all nucleolar proteins in our experiments is expected to change correspondingly, i.e. $C_{n,i} = \zeta_i C_n$, where i indicates a given nucleolar component whose concentration relative to that of fibrillarin is given by the stoichiometric coefficient ζ_i. However, it is possible that the composition of the nucleolus is not fixed throughout development or across RNAi conditions, such that the relative amount of a given component may vary with respect to fibrillarin. Indeed, the concentration of DAO-5 does not depend as strongly on embryo volume as expected (Figure S2D). Nevertheless, maternal loading of an intact nucleolus into oocytes of different size represents a useful experimental tool to tune the concentration of the majority of nucleolar components in a simple, concerted fashion.

Developmental parameter, χ:

We find qualitatively different nucleolar behavior at the 4-cell stage compared to subsequent stages. While nucleoli readily assemble in 8-cell stage nuclei and beyond, they rarely appear in WT embryos at the 4-cell stage (Table S1). When they do assemble, in cell EMS, nucleoli are small and do not scale with nuclear volume according to the same relationship as later stages. Nucleoli do not appear in cells ABa and ABp, despite the fact that $C_n > C_{sat}$. However, increasing the nucleoplasmic concentration further, either by decreasing embryo volume (*ima-3(RNAi)*) or by increasing the number of nucleolar components (*ncl-1(e1942)*), we can induce nucleolar assembly in these cells. Therefore, nucleolar assembly still depends on concentration but the saturation threshold is higher: $C_{sat}^{4\text{-cell}} > C_{sat}$.

Phase transitions are controlled by the thermodynamic properties of the system. For example, in the condensation of water vapor into droplets on a cold mirror, temperature is the relevant variable. However, in a biological context, molecular concentrations or the degree of post-translational modifications are more appropriate variables. Thus, we hypothesize that an interaction parameter, χ, and therefore C_{sat}, may be developmentally regulated through a post-translational modification that renders key nucleolar components more or less likely to interact with itself or other nucleolar components.

Supplemental References

S1. Hara, Y., and Kimura, A. (2009). Cell-size-dependent spindle elongation in the *Caenorhabditis elegans* early embryo. Curr. Biol. *19*, 1549–1554.

S2. Sarov, M., Murray, J. I., Schanze, K., Pozniakovski, A., Niu, W., Angermann, K., Hasse, S., Rupprecht, M., Vinis, E., Tinney, M., et al. (2012). A genome-scale resource for *in vivo* tag-based protein function exploration in *C. elegans*. Cell *150*, 855–866.

S3. Green, R., Audhya, A., Pozniakovsky, A., Dammernmann, A., Pemble, H., Monen, J., Portier, N., Hyman, A., Desai, A., and Oegema, K. (2008). Expression and imaging of fluorescent proteins in the *C. elegans* gonad and early embryo. Methods Cell Biol. *85*, 179–218.

S4. Praitis, V., Casey, E., Collar, D., and Austin, J. (2001). Creation of low-copy integrated transgenic lines in *Caenorhabditis elegans*. Genetics *157*, 1217–1226.

S5. Pologruto, T. A., Sabatini, B. L., and Svoboda, K. (2003). ScanImage: Flexible software for operating laser scanning microscopes. Biomed Eng Online *2*, 13.

S6. Kamath, R. S., Fraser, A. G., Dong, Y., Poulin, G., Durbin, R., Gotta, M., Kanapin, A., Le Bot, N., Moreno, S., Sohrmann, M., et al. (2003). Systematic functional analysis of the *Caenorhabditis elegans* genome using RNAi. Nature *421*, 231–237.

S7. Geles, K. G., and Adam, S. A. (2001). Germline and developmental roles of the nuclear transport factor importin α3 in *C. elegans*. Development *128*, 1817–1830.

S8. Brangwynne, C. P., Mitchison, T. J., and Hyman, A. A. (2011). Active liquid-like behavior of nucleoli determines their size and shape in *Xenopus laevis* oocytes. Proc. Natl. Acad. Sci. U.S.A. *108*, 4334–4339.

S9. Marshall, W. F. (2011). Centrosome size: scaling without measuring. Curr. Biol. *21*, R594–6.

S10. Goehring, N. W., and Hyman, A. A. (2012). Organelle growth control through limiting pools of cytoplasmic components. Curr. Biol. *22*, R330–9.

S11. Zipfel, W. R., Williams, R. M., and Webb, W. W. (2003). Nonlinear magic: multiphoton microscopy in the biosciences. Nat Biotechnol *21*, 1369–1377.